Millimeter-Wave Beam Scattering and Induced Broadening by Plasma Turbulence in the TCV Tokamak

O. Chellaï,[1,3] S. Alberti,[1] I. Furno,[1] T. Goodman,[1] O. Maj,[2] G. Merlo,[4] E. Poli,[2] P. Ricci,[1] F. Riva,[5] H. Weber,[2] and the TCV team[1]

[1] *Swiss Plasma Center (SPC), École Polytechnique Fédérale de Lausanne (EPFL), Lausanne, Switzerland*
[2] *Max Planck Institute for Plasma Physics, Garching, Germany*
[3] *Princeton Plasma Physics Laboratory, Princeton, New Jersey 08543, USA*
[4] *Institute for Fusion Studies, University of Texas at Austin, Austin, USA*
[5] *Istituto Ricerche Solari Locarno (IRSOL), 6605 Locarno Monti, Switzerland*

The scattering of millimeter-wave beams from electron density fluctuations and the associated beam broadening are experimentally demonstrated. Using a dedicated setup, instantaneous deflection and (de-)focusing of the beam due to density blobs on the beam path are shown to agree with full-wave simulations. The detected time-averaged wave power transmitted through the turbulent plasma is reproduced by the radiative-transfer model implemented in the WKBeam code, which predicts a $\sim 50\%$ turbulence-induced broadening of the beam cross-section. The role of core turbulence for the considered geometry is highlighted.

In magnetic fusion devices [1–4], millimeter-wave (mmw) beams in the electron cyclotron (EC) range of frequencies are used for plasma diagnostics [5], heating and current drive [6], and to stabilize magneto-hydrodynamic instabilities like the neoclassical tearing mode (NTM) [7, 8]. Density fluctuations, associated with plasma turbulence on the path of the mmw beam, result in local fluctuations of the mmw power that can lead to difficulties in diagnostic interpretation [9] and to potential degradation of the EC current-drive efficiency [10]. EC-beam broadening associated with the scattering of mmw from plasma turbulence is predicted for ITER [11], which could hamper its NTM stabilization capabilities [1]. However, direct experimental evidence is still missing. From the theory point of view, although Maxwell's equations coupled to the cold-plasma model would provide an adequate description of the wave propagation away from cyclotron resonances, the sheer number of degrees of freedom required for 3D full-wave simulations makes the approach impractical. Therefore, identifying the essential physics processes that contribute to the macroscopic wave-energy transport has been a long-standing issue in the field of nuclear fusion [10–15].

In this paper, we report first direct experimental measurements of mmw beam broadening and associated scattering by plasma turbulence in the Tokamak à Configuration Variable (TCV) [16]. A high-power mmw beam is launched from the top of the TCV vessel through a limited L-mode plasma. A receiving antenna attenuates and measures the mmw-beam power arriving at the bottom of the vessel [17]. This dedicated setup maximizes both the distance between the launching position and the detector as well as the path through the plasma, making the beam broadening due to plasma turbulence, and core turbulence in particular, directly measurable for the first time in a fusion device. Using Langmuir probe (LP) data, we show that filaments or blobs intercepting the mmw beam induce fluctuations in the detected power by instantaneously deflecting and (de-)focusing the beam, in agreement with full-wave simulations, similarly to previous observations made in basic plasma physics devices [18]. Most notably, using experimentally validated GBS fluid simulations [19] of the plasma edge and GENE [20, 21] gyro-kinetic simulations of the plasma core, we compare the time-average measured mmw-power profile with the one computed using the WKBeam code [22]—a Monte-Carlo solver for the wave kinetic equation. We show that plasma turbulence is responsible for a broadening of the time-averaged beam cross-section of $\sim 50\%$, which can be attributed mostly to core turbulence. The successful comparison between the experiments and the WKBeam simulations provides a direct experimental test for the physics assumptions at the basis of the reduced radiative transfer model that is employed for the description of the macroscopic wave-energy transport.

EXPERIMENTAL SETUP

A TCV elongated (elongation $\kappa = 1.52$) ohmic L-mode deuterium plasma is generated with a toroidal magnetic field on axis $B_T = 1.41$ T. The magnetic geometry is shown in Fig. 1(a). The time-averaged electron density profile from the Thomson scattering (TS) diagnostic [23] is shown as a function of the normalized flux coordinate ρ_ψ in Fig. 1(b). The central electron density is $n_e \approx 7.3 \times 10^{19} m^{-3}$, while $n_e \approx 6 \times 10^{18} m^{-3}$ at the last-closed-flux surface (LCFS). Drift-waves and ballooning modes are responsible for driving turbulence at its edge [24, 25] associated with local fluctuations of the electron density and thus of the dielectric permittivity. Figure 1(c) shows the ion saturation current $I_{\rm sat} \propto n_e$ [26, 27] measured by the LP [28] shown in Fig. 1(a). The fluctuations of $I_{\rm sat}$ are associated

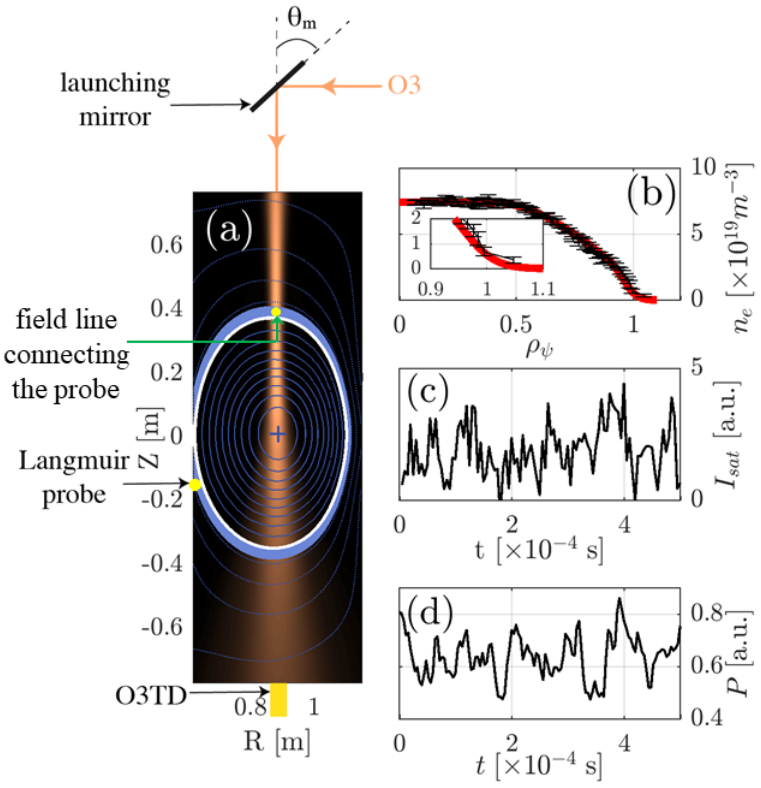

FIG. 1. (a) An O-mode mmw beam (copper-shaded area) is launched through a limited L-mode plasma, represented by its flux surfaces (contours). The blue shaded area covers the SOL region between the LCFS and the location where the density has dropped to half of its value at the LCFS. The transmitted mmw-power (d) is measured using the O3TD diagnostic. (b) Time-averaged electron density profile from the TS diagnostic and fit to the experimental data (red). The insert is a zoom of the edge region. (c) Time evolution of the ion saturation current measured at the probe location shown in (a).

with the presence of field-aligned plasma filaments at the edge of the plasma [29]. To mimic the ITER upper launcher scheme, the third harmonic EC-wave (100 kW, frequency 117.8 GHz, vacuum wavelength $\lambda = 2.5$ mm) is launched in the ordinary mode from the top of the vessel through the plasma using a steerable focusing mirror. The beam waist (e-folding length of the $E-$field) in vacuum for a vertical launch of the beam is $w = 17.60$ mm in the $R-$direction and is located at [$R = 0.88$ m, $Z = 0.36$ m]. A transmission diagnostic (O3TD)[30] was developed and installed at the location [$R = 0.88$ m , $Z = -0.77$ m], displayed in Fig. 1(a) [17]. The receiving antenna is made of an HE_{11} circular waveguide (63.5 mm diameter) topped with an array of 241 circular holes (with a cut-off frequency for the lowest order TE_{11} circular mode of $f_c = 146.4$ GHz) acting as a -55 dB attenuator. The mmw-power collected by the antenna is coupled to a WR 6.5 rectangular waveguide, oriented in the ordinary-mode, through a lens horn antenna and is measured by a Schottky diode. The measured mmw-power P coupled to the O3TD antenna is shown in black in Fig. 1(d). The level of fluctuation is $\approx 20\%$ and is partly caused by n_e changes associated with the core sawtooth activity and, as will be detailed later, by plasma turbulence.

INSTANTANEOUS EFFECT OF BLOBS ON THE MMW BEAM

We first show that turbulent structures localized at the edge of the plasma are responsible for *instantaneous* fluctuations of the measured mmw-power.

Verifying the field-aligned nature of the blobs in TCV

We confirm the field-aligned nature of the blobs by varying the plasma current (and thus the tilt of the magnetic field lines). Whether or not a blob detected by a Langmuir probe crosses the path of the mmw beam depends on the location of the intersection between the magnetic field line connecting the probe and the plane of the mmw beam (see Fig. 2(a)). This intersection is shown in Fig. 2(a) and can be controlled by changing the tilt of the magnetic field line and thus by varying the plasma current I_p. We investigate the influence of I_p on the maximum of the correlation function $|C_0|_{max}$ of the detected mmw-power signal $P(t)$ and the $I_{sat}(t)$ signal measured by the probe shown in Fig. 1(a) and the corresponding time lag δt_{max} in Fig. 2(b) and (c)). The errorbars are given by the uncertainty in the estimate of $|C_0|_{max}$ and are equal to $\frac{1-|C_0|^2_{max}}{\sqrt{N}}$, were $N \sim 2000$ [31]. Figure 2(b) shows that $|C_0|_{max}$ *increases* for I_p ramping from -278 kA to -271 kA — the intersection is moving to the center of the mmw beam — where it reaches its maximum value. The seemingly low value of 0.14 is explained by the fact that a blob detected by the Langmuir probe contributes only partly to the mmw-signal fluctuations. The value of $|C_0|_{max}$ then *decreases* for I_p ramping up from -271 kA to -260 kA — the intersection, and thus the detected blob, is moving away from the center of the beam. For $I_p > -260$ kA, the I_{sat} signal from the probe no longer exhibits a significant level of correlation to the P signal ($|C_0|_{max} < 0.06$) and the intersection is far away from the beam path.

Figure 2(c) shows that the time lag δt_{max} decreases linearly, from $\delta t_{max} = +4$ μs to $\delta t_{max} = -44$ μs, when I_p increases from -278 kA to -260 kA. When δt_{max} is negative (positive), the turbulent structure affects the mmw propagation before (after) being detected by the Langmuir probe. From the values of $\delta t_{max}(I_p)$ and the knowledge of the position of the intersection between the corresponding field line and the path of the beam, we

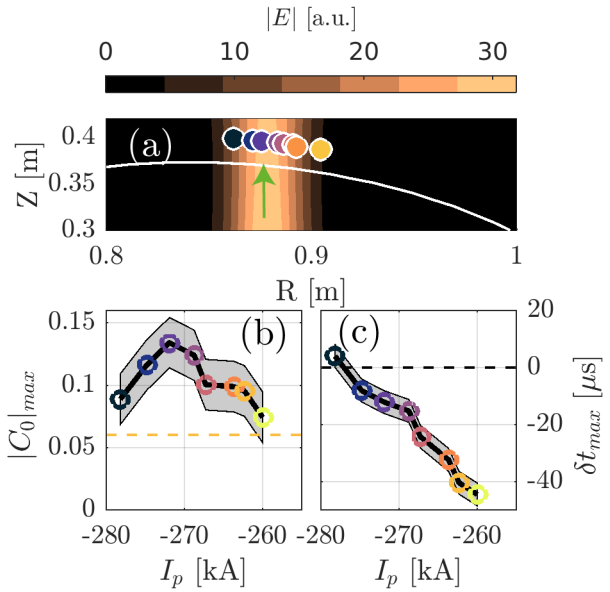

FIG. 2. Correlation between P and I_{sat}. (a) The colored circles represent the intersection of the field lines connecting the Langmuir probe and the mmw beam (the amplitude of the associated electric field amplitude is given by the copper-shaded surface) at the plasma currents shown in (b) and (c). The white line represents the last closed flux surface. (b) Maximum of the cross-correlation function between P and I_{sat} measured by the Langmuir probe as a function of the plasma current. The level $|C_0|_{max}$ above which the correlation is considered significant is indicated by the yellow dashed line. (c) Time lag at which the maximum level of cross-correlation given in (b) occurs. The errorbars (gray area) in (a) are given by the statistical uncertainty in the estimate of $|C_0|_{max}$ and in (b) by the sampling period of the signals.

deduce a quasi-poloidal speed v associated with the motion of the structure $|\mathbf{v}| \approx 0.9$ km·s^{-1} directed clockwise. This is found to be in good agreement with measurements performed with a fast-reciprocating probe [32, 33].

Effect of a typical blob on the mmw beam

To elucidate the effect of a typical blob on the mmw beam, we perform conditional sampling (CS) [34] on P and $I_{\rm sat}$ over $N \approx 300$ blob events with a time window centered around each event. Events are defined as local maxima fulfilling the condition $I_{\rm sat} > \langle I_{sat}\rangle + 2\sigma$ with $\langle I_{sat}\rangle$ and σ being respectively the time-averaged value and the standard deviation of $I_{\rm sat}$ calculated over the entire time trace. All quantities obtained with CS are labeled with a tilde, except τ which is the time relative to the blob event, $\tau = 0$ μs corresponding to the detection of the blob. The LP shown in Fig. 1(a) is used for blob detection. This is equivalent to detecting a blob passing by the location $[R = 0.88$ m$, Z = 0.4$ m$]$ at $\tau = 0$ μs. The result of CS of the detected mmw-power is presented in Fig. 3(a). They show that the conditionally-sampled blob increases the mmw-power transmitted to the O3TD antenna at $\tau = -50$ μs and decreases it at $\tau = -14$ μs. The resulting level of fluctuation $\delta\tilde{P}/\langle P\rangle$ is $\sim 8\%$.

Comparison with full-wave simulations

To understand the deflection of the beam due to a blob intersecting the beam path, we perform numerical simulations. "Various methods are currently available for the description of wave beams in fusion plasmas [36]. However, since the typical blob size L_b is comparable to or even smaller than the beam width w, standard beam-tracing methods [35] do not apply. In our experiments, the blob size compared to the wavelength gives $L_b/\lambda \sim 4$ which could be considered large enough for ray tracing methods [36] to apply [12], but ray tracing methods cannot account for diffraction effects [46]. Moreover in a turbulent plasma there is a finite probability to have blobs of size smaller than the average L_b, thus violating the validity conditions of ray tracing. In this case, a more recent generalization of the ray- or beam-tracing approach [10] or a full-wave model is needed. We use 2D full-wave simulations [17, 18] based on COMSOL MULTIPHYSICS [37]. The absorption being negligible in our experiments, the dielectric permittivity of the plasma is computed from the cold-plasma model and depends on $n_e(\mathbf{x}, t)$ and $\mathbf{B}(\mathbf{x})$ [38], where t is frozen. The equilibrium $\langle n_e(\mathbf{x})\rangle$ is taken from the TS data and $\mathbf{B}(\mathbf{x})$ from the equilibrium code LIUQE. CS is applied to $\delta n_e(\mathbf{x}, t) = n_e(\mathbf{x}, t) - \langle n_e(\mathbf{x})\rangle$ from the GBS simulations to reconstruct the 2D evolution of $\delta\tilde{n}_e(\mathbf{x}, t)$ associated with the blob propagation. The reference signal $\delta n_e(\mathbf{x}_0, t)$ is used, where $\mathbf{x}_0$ is the location of the GBS grid point in the poloidal plane corresponding to the location $[R = 0.88$ m$, Z = 0.4$ m$]$ mentioned before. Two snapshots of $\delta\tilde{n}_e$ are shown in Fig. 3(b) and (c). The conditionally-sampled blob has a typical full-width half-maximum size $L_b \approx 1$ cm in the direction transverse to the magnetic field and a quasi-poloidal rotation motion with a velocity of $|\mathbf{v}| \approx 0.92$ km $\cdot$ s^{-1}, in agreement with the value of $|\mathbf{v}| \approx 0.9$ km·s^{-1} found previously.

As in the experiments, the numerical beam is launched vertically. The simulations are performed at 15 CS times τ_i, with $\delta\tau = \tau_{i+1} - \tau_i = 10$ μs. Figure 3(b) and (c) show the fluctuations of the conditionally-sampled electric field amplitude $\delta|\tilde{\mathbf{E}}(\mathbf{x}, \tau)| = |\tilde{\mathbf{E}}(\mathbf{x}, \tau)| - \langle|\mathbf{E}(\mathbf{x})|\rangle$ of the mmw beam caused by the propagation of the blob. In Fig. 3(b), $\delta\tilde{n}_e < 0$ preceding the blob is responsible for the focusing of the mmw beam, resulting in an increase of mmw power at the location of the O3TD diagnostic. Later (Fig. 3(c)), the blob with $\delta\tilde{n}_e > 0$ causes a defocusing of the mmw beam behind the blob, on the receiver side, decreasing $\delta\tilde{P}$. These observations are in agreement with those previously made in a simple magnetized torus

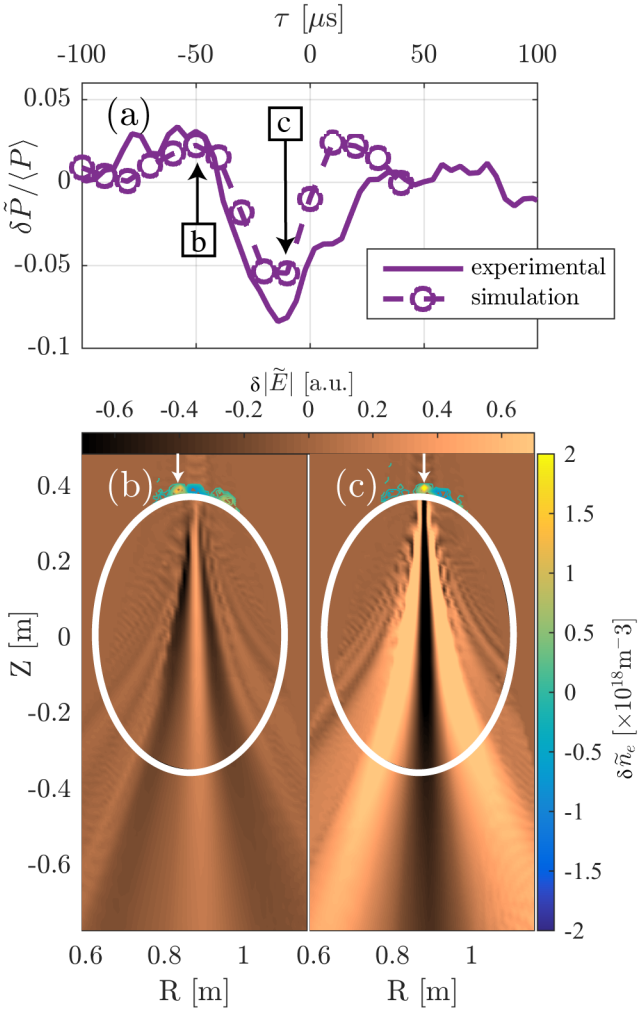

FIG. 3. (a) CS time evolution of the detected mmw-power (solid line) using the LP shown in Fig. 1(a). Experimental results (solid line) are compared to numerical simulations (dashed line). (b) and (c) Snapshots of the fluctuation of the electric field norm resulting from the propagation of the blob (indicated by the white arrow) at the times indicated in (a). The white contour is the LCFS. (b) A structure with $\delta\tilde{n}_e < 0$ preceding the blob focuses the mmw beam. (c) The blob defocuses the mmw beam.

[18]. The resulting $\delta\tilde{P}/\langle P\rangle$ is shown in Fig. 3(a) and is successfully compared with the experimental measurements, suggesting concomitantly a correct description of the SOL turbulence by the GBS code.

TIME-AVERAGED EFFECT OF PLASMA TURBULENCE ON THE MMW BEAM PROFILE

We turn now to the *time-averaged* effect of plasma turbulence on the beam profile. To this goal, experiments are performed where the poloidal angle of the launching mirror is swept from $\theta_m = 44°$ to $\theta_m = 46°$, with $\theta_m = 45°$ corresponding to the vertical launch of the beam. To ensure that the variations of $n_e(\mathbf{x}, t)$ associated with the sawtooth oscillations do not affect the $P(\theta_m)$ profile, P is averaged in a 0.5 ms time window occurring 1 ms after the sawtooth crash, longer than the autocorrelation time ($\sim 10^{-5}$ s) of the turbulence. During this time interval, $\Delta\theta_m \sim 0.001\,°$ and $(\Delta n_e/n_e)_{\text{sawtooth}} < 1\%$. In Fig. 4(a), $P(\theta_m)$ is shown and fitted by a Gaussian (in black) $P(\theta_m) = Ae^{-2(\frac{\theta_m-\theta_0}{w_\theta})^2}$ with a width of $w_{\theta,\text{exp}} = 0.94°$.

WKBeam simulations for the mmw beam propagation

The $P(\theta_m)$ profile is compared to the one computed by the WKBeam code [22], which was successfully benchmarked against full-wave codes [17, 39] and validated in vacuum against experiments [17]. The WKBeam code solves a radiative transfer model for the wave energy density, accounting for refraction, diffraction, resonant damping and scattering by density fluctuations of arbitrary spatial size under the Born approximation [39, 40]. Time-dependent density fluctuations are modeled as a time-independent random density field. Time-averages of relevant physical observables are computed as ensemble-averages (ergodic hypothesis). The scattered wave is represented by a Born series truncated to the lowest order (Born approximation). Remarkably, the resulting equation for the wave-field correlation can be analyzed by means of the Wigner-Weyl transform in the short-wavelength limit, even though the fluctuations have finite probability to generate short-scale structures, since this limit is applied to the equation for the field correlation, not to the wave field directly. Similarly to the full-wave simulations, mmw beam and plasma parameters are taken from the experiments. For scattering, the WKBeam code requires two functions of the coordinates (ρ_ψ, θ) in the poloidal plane—ρ_ψ being the normalized flux coordinate and θ the poloidal angle with $\theta = 0, \frac{\pi}{2}$ on the low-field side and upward vertical from the magnetic axis, respectively: the relative r.m.s. of electron density fluctuations $\delta n_{e,\text{rms}}/\langle n_e\rangle$ and the perpendicular correlation length $L_\perp$, defined by $\langle \delta n_e(\mathbf{x} + \frac{\mathbf{s}}{2})\delta n_e(\mathbf{x} - \frac{\mathbf{s}}{2})\rangle \propto \exp(-\frac{|\mathbf{s}_\perp|^2}{2L_\perp^2})$ where $L_\perp$ is evaluated at the coordinates (ρ_ψ, θ) of the point $\mathbf{x}$ and $\mathbf{s}_\perp = \mathbf{s} - (\mathbf{b}\cdot\mathbf{s})\mathbf{b}$, $\mathbf{b} = \mathbf{B}(\mathbf{x})/B(\mathbf{x})$. These two functions are constructed from the simulations used above based on the GBS code [41] in the SOL, and from gyro-kinetic simulations with the GENE code [21, 42] in the core. In the GBS domain defined by $1.01 \le \rho_\psi < 1.11$, simulations allow us to reconstruct the values of $\delta n_{e,\text{rms}}/\langle n_e\rangle$ on a regular grid in (ρ_ψ, θ) which are then interpolated. In the core region, $\rho_\psi \le \rho_c = 0.8$, GENE simulations give $\delta n_{e,\text{rms}}/\langle n_e\rangle$ for three values of ρ_ψ and $\theta = \frac{\pi}{2}$, shown in Fig. 4(b). There-

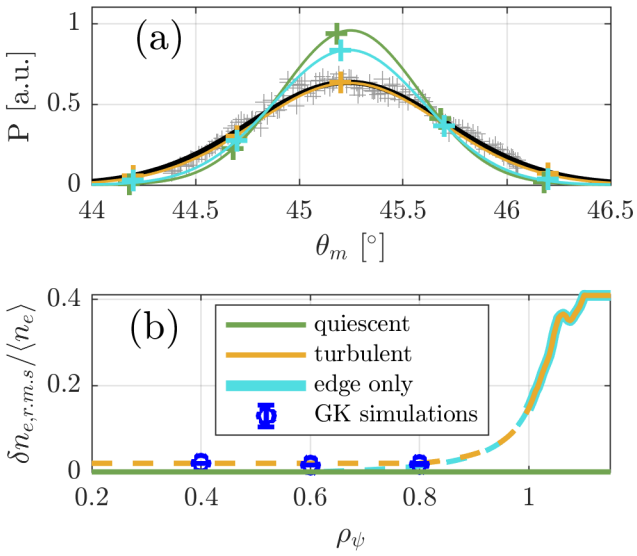

FIG. 4. (a) Comparison between the measured mmw-power (gray crosses) as a function of the injection mirror angle θ_m and results from WKBeam simulations. The black line is a Gaussian fit to the experimental measurements. (b) Profiles of the electron density fluctuation level from the GBS simulations. The profiles are extrapolated for $\rho_\psi < 1$ as explained in the text. Results from gyrokynetic simulations are shown in dark blue.

fore a constant value of 2% is chosen to match GENE results for $\rho_\psi \leq \rho_c$, and that is connected to the interpolated GBS data by means of an analytical model guided by reflectometry measurements [43, 44]. In addition, we also consider another profile, labeled "edge only", in which $\delta n_{e,\mathrm{rms}}/\langle n_e \rangle = 0$ in the core so that only the edge fluctuations are accounted for. These profiles and data are shown in Fig. 4(b) for $\theta = \frac{\pi}{2}$. As for $L_\perp$, WKBeam simulations have been performed with different constant values of $L_\perp$, namely $L_\perp = 0.4,\ 1$ and 1.4 cm matching the GENE estimates ($L_\perp = 1.01, 1.39, 0.42$ cm at $\rho_\psi = 0.4, 0.6, 0.8$, respectively), as well as with $L_\perp \propto \rho_s$ where ρ_s is the sound Larmor radius, which is a function of (ρ_ψ, θ), and the proportionality constant is fitted. For comparison we also consider a "quiescent" plasma, i.e. $\delta n_{e,\mathrm{rms}} = 0$.

Evidence of mmw-beam broadening due to plasma turbulence

For each injection angle, WKBeam computes the power flux coupled to the O3TD antenna. The WKBeam profiles are normalized so that the amplitude of the turbulent case matches the experimental one ($A_{\mathrm{turb}} = A_{\mathrm{exp}}$). The profiles are shown in Fig. 4(b) for $L_\perp = 1$ cm (which matches the GENE estimate in the core) and compared to the experimental measurements. We find that the width of the WKBeam profile computed for the "'turbulent" case ($w_{\theta,\mathrm{turb}} = 0.90°$) is in good agreement with the experimental one ($w_{\theta,\mathrm{exp}} = 0.94°$). The two WKBeam profiles obtained for the "quiescent" and "edge only" cases are narrower ($w_\theta \approx 0.66°$ and $w_\theta \approx 0.73°$, respectively) and are not in agreement with the experimental one. The difference is due to a broadening of the mmw beam associated with the scattering from plasma turbulence occurring along the path of the beam. We find that the WKBeam profile is sensitive to changes of the core value of $\delta n_{e,\mathrm{rms}}/\langle n_e \rangle$, but depends weakly on $L_\perp$, in the considered range. The profile obtained with $L_\perp \propto \rho_s$ is also very close to that of Fig. 4(a). Indeed, the variable $L_\perp$ model evaluates to ≈ 1 cm for small ρ_ψ. To our knowledge, this is the first direct experimental measurement of this effect for EC wave beams in tokamak plasmas. At the same time, these results also allow for the first time a validation of the WKBeam model against experiments. The angle sweep of the launching mirror is intended to test the accuracy of both the central trajectory of the beam and the width of its cross-section: For different angles the detector is sensitive to a different area of the beam cross-section. Furthermore, the experimental data are time-averaged and compared to the ensemble average computed by the WKBeam code. The experiment has therefore the potential to detect inaccuracies in either the beam trajectory (refraction) or width (diffraction and scattering), and to test the equivalence of time and ensemble averages (ergodic hypothesis). We observe a good agreement between data and numerical model, and thus conclude that the WKBeam code passed this specific validation test. From this result however, we can draw no conclusion on each of the basic physics assumptions individually – (i) the ergodic hypothesis, (ii) the Born scattering approximation, and (iii) the short-wavelength limit – but only on the WKBeam model as a whole, including the density-correlation model (which has been carefully constrained by simulations and measurements).

DISCUSSION OF THE RESULTS AND COMPARISON WITH ITER

The role of core turbulence in broadening the mmw beam in TCV seems to contradict previous ITER studies [10] which show that edge turbulence is mainly responsible for the scattering of the beam under conditions typical for NTM stabilization. This difference is a consequence of the different plasma parameters and propagation paths in both machines and can be understood employing an analytical expression for the beam width obtained in slab geometry [45], whose derivation is sketched

in the appendix. The squared beam width reads

$$w^2(\tau) = w^2_{\rm GB}(\tau) + \int_0^\tau \frac{1}{L_\perp}\sqrt{\frac{2\pi}{\varepsilon_0}}\left\langle\frac{\delta n_e^2}{n_{e,c}^2}\right\rangle(\tau-\tau')^2 d\tau', \quad (1)$$

where τ is a parameter related to the arc-length ℓ of the beam path by $d\ell = \sqrt{\varepsilon_0}d\tau$, $\varepsilon_0 = 1 - n_e/n_{e,c}$ $n_{e,c}$ being the O-mode cut-off density, and $w_{\rm GB}$ is the standard width of a Gaussian beam in slab geometry without turbulence [46]; both $L_\perp$ and $\langle\delta n_e^2\rangle$ can depend on the position along the beam path. Eq. (1) has been obtained by Sysoeva et al. [15] with different methods and it is recovered here directly from the analytical solution of the WKBeam model specialized to the case of O-mode propagation in slab geometry, thus proving that these two different theories yield the same conclusion on the beam broadening.

Eq. (1) captures the fundamental dependencies of the turbulence-induced beam broadening. To estimate the relative importance of core and edge turbulence for the beam broadening, in Fig. 5 we show the integrand in the last term of Eq. (1) times $d\tau'/d\ell'$, which gives the scattering contribution per unit arc-length, as a function of the radial coordinate ρ. The plasma parameters are evaluated on the central ray of WKBeam simulations and the integrand of Eq. (1) is computed for τ corresponding to the last point along the ray (in TCV, this is the position of the detector at the bottom of the machine, while in ITER it is the position at which the power on the central ray is completely absorbed). It can be appreciated that the contribution from the core is significantly larger than the contribution of the edge for TCV (the height of the peaks of the integrand is roughly comparable in the core and in the edge, but in the core region the peak is much broader and the path much longer). On the contrary, for ITER the edge is responsible for most, if not all, the beam scattering, in agreement with the results of [10] (see Fig. 10 and Fig. 1 in [10] for, respectively, the radial profiles of density and density fluctuations assumed for ITER). In fact, the ITER beam is absorbed on the rational surface of interest outside $\rho \simeq 0.85$, without further penetrating in the plasma, as shown also by the upper inset. The core fluctuations thus contribute to the scattering on a significantly shorter path in ITER as compared to TCV. To better appreciate the results displayed in Fig. 5, two further comments can be made. With reference to the TCV curve, it can be observed that scattering from regions which are more distant from the observation point contributes more strongly to the beam broadening, since the scattered radiation propagates then on a longer path. Mathematically, this is expressed by the factor $(\tau - \tau')^2$ in Eq. (1). Thus the higher values of the integrand for a given ρ in Fig. 5 correspond to the first crossing (closer to the injection point) of that radial position, while lower values correspond to the crossing closer to the final point. Finally, the two-peak structure

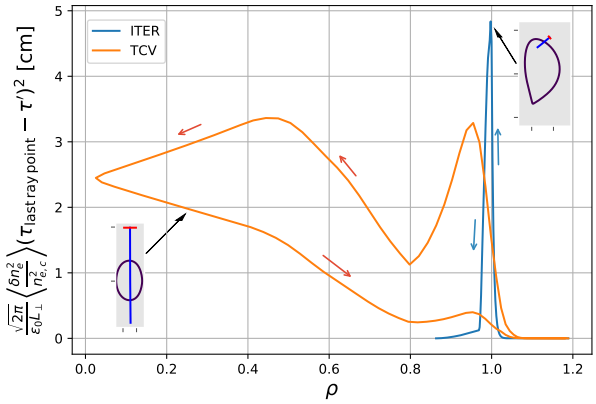

FIG. 5. Integrand in the last term of Eq. (1) as a function of the radial coordinate ρ for TCV (present paper) and ITER [10]. The plasma parameters are calculated along the central ray of WKBeam simulations. The doubled-value structure of the TCV curve is due to the fact that the same radial position is crossed twice (lower values correspond to positions closer to the observation point). The arrows show the propagation direction, starting from the launching mirror.

of the integrand can be explained by the fact that according to the formula the strongest contributions to the scattering occur either where the relative fluctuation amplitude $\langle\delta^2 n_e/n_e^2\rangle$ is highest (peak at the edge) or where the background density $n_e^2/n_{e,c}^2$ is highest, or in other words closest to cutoff (peak in the centre).

As a concluding remark, we stress here that Eq. 1, while correctly capturing the scalings of the beam width with the various plasma parameters, cannot be employed for a quantitative assessment, mainly because of the simplifying assumptions on the plasma geometry [45]. For a quantitative comparison with the experiments, WKBeam simulations as described above are needed.

CONCLUSION

In summary, we presented the first evidence of mmw scattering and turbulent broadening in a tokamak using a combination of *in-situ* measurements of the electron density and experimentally validated plasma turbulence simulations. In TCV, instantaneous deflections of the beam due to the presence of edge blobs, inducing fluctuations of the mmw power of the order of $\sim 10\%$ have been demonstrated. Most notably, using a dedicated setup, we measured directly and for the first time a $\sim 50\%$ turbulence-induced broadening of the time-averaged cross-section of a beam traversing vertically the TCV plasma column. All these results agree with numerical simulations based on a combination of turbulence codes and wave-equation solvers, confirming the reliability of the theoretical approach and, in particular, the validity of the underlying physics assumptions of WKBeam.

Differences between different injections scenarios (e.g. TCV and ITER) are explained on the basis of the developed model.

The authors acknowledge useful discussions with Kate Sysoeva and the first author would like to thank S. Coda for his support on the planning of the experimental sessions on TCV. This work has been carried out within the framework of the EUROfusion Consortium and has received funding from the Euratom research and training programme 2014-2018 and 2019-2020 under grant agreement No 633053. The views and opinions expressed herein do not necessarily reflect those of the European Commission. The views and opinions expressed herein do not necessarily reflect those of the European Commission. This work was supported in part by the Swiss National Science Foundation.

APPENDIX: ANALYTICAL EXPRESSION OF THE BEAM WIDTH IN TURBULENT PLASMAS

In this section, we sketch the main steps and summarize the main approximations leading to an analytic formula for the beam width in the presence of scattering from density fluctuations, Eq. (12) below, which is Eq. (1) in the body of the paper. It is obtained in the frame of the same theoretical approach as implemented in the code WKBeam. A complete derivation and a detailed discussion is out of scope here and will be reported elsewhere [45]. Upon neglecting absorption at the electron-cyclotron resonance, the radiative transfer model solved by the WKBeam code [22] amounts to a constrained steady state kinetic equation,

$$\big\{H, W\big\} = S(W), \qquad HW = 0, \tag{2}$$

where the unknown $W = W(\mathbf{x}, \mathbf{N})$ is the Wigner function of the wave electric field defined over the position ($\mathbf{x}$) and refractive index ($\mathbf{N}$) phase-space. The function

$$H(\mathbf{x}, \mathbf{N}) = N^2 - |\mathbf{N}\cdot\mathbf{e}|^2 - \mathbf{e}^*\boldsymbol{\varepsilon}\mathbf{e}, \tag{3}$$

is the geometric-optics Hamiltonian defined in terms of the cold-plasma dielectric tensor $\boldsymbol{\varepsilon}$ [38] and the polarization unit vector of the wave electric field $\mathbf{e}$ for the considered mode (either ordinary (O) or extra-ordinary (X) mode); by $\mathbf{e}^*$ we denote the Hermitian conjugate of the complex vector $\mathbf{e}$. In addition, $\{\cdot,\cdot\}$ is the Poisson bracket defined, for any pair (f, g) of phase-space functions, by $\{f, g\} = \nabla_{\mathbf{N}} f \cdot \nabla_{\mathbf{x}} g - \nabla_{\mathbf{x}} f \cdot \nabla_{\mathbf{N}} g$, and

$$S(W) = \int \sigma(\mathbf{x}, \mathbf{N}', \mathbf{N}) \times \big[W(\mathbf{x}, \mathbf{N}')\delta(H) - W(\mathbf{x}, \mathbf{N})\delta(H')\big] d^3N', \tag{4}$$

is the scattering operator which accounts for the effect of density fluctuations. Here, $\delta(H)$ (resp., $\delta(H')$) denotes the Dirac's measure concentrated on the dispersion surface $H = 0$, (resp., $H' = 0$, where $H' = H(\mathbf{x}, \mathbf{N}')$ is the Hamiltonian evaluated at $\mathbf{N}'$); the products with the (singular) Wigner function are well defined as direct products of distributions. The scattering cross section,

$$\sigma(\mathbf{x}, \mathbf{N}, \mathbf{N}') = \frac{k_0^4}{(2\pi)^2} \frac{\big|\mathbf{e}^*(\boldsymbol{\varepsilon} - I)\mathbf{e}\big|^2}{n_e^2} \Gamma(\mathbf{x}, \mathbf{N} - \mathbf{N}'),$$

depends on the Wigner-Weyl transform Γ of the two-point correlation function $\langle \delta n_e(\mathbf{x}) \delta n_e(\mathbf{x}') \rangle$ of the random density fluctuations δn_e. Here angle brackets denote ensemble average, I the identity tensor, $k_0 = \omega/c$ is the wave number in free space, and n_e the equilibrium electron density. We refer the reader to the review paper by McDonald [47] for the definition of Wigner functions, Weyl symbols, and related mathematical results, on which we do not digress for sake of brevity.

We consider a plasma-slab geometry with a Cartesian coordinate system (x, y, z) such that the density is $n_e = n_e(x)$, and the constant magnetic field is directed along the z-axis. In the slab a beam is launched with O-mode polarization and in the limit of perpendicular propagation, hence $N_\parallel \approx 0$ and $\mathbf{e} \approx (0, 0, 1)$.

Adopting a Gaussian *ansatz* for the two-point correlation function of the density fluctuations and taking the limit of very large parallel correlation length, we can write following the same steps as detailed in [10]

$$\sigma(\mathbf{x}, \mathbf{N}, \mathbf{N}') \approx k_0^3 L_\perp^2 \Big\langle \frac{\delta n_e^2}{n_{e,c}^2} \Big\rangle e^{-\Delta N_\perp^2/(2\nu_\perp^2)} \delta(\Delta N_\parallel), \tag{5}$$

where $\Delta N_\perp^2 = (N_x - N_x')^2 + (N_y - N_y')^2$, $\Delta N_\parallel = N_z - N_z'$, and $\nu_\perp = 1/(k_0 L_\perp)$.

As a last simplification, we restrict our analysis to beams that are paraxial and experience no cut-off.

In this limit, the Hamiltonian (3) is

$$H = 2\xi + \xi^2/\varepsilon_0 + \eta^2 \approx 2[\xi + h(\eta)], \tag{6}$$

with $\xi = \sqrt{\varepsilon_0(x)}(N_x - \sqrt{\varepsilon_0(x)})$, $\eta = N_y$ and where $h = \eta^2/2$ plays the role of a reduced Hamiltonian. In the paraxial limit, we can neglect the $(N_x - N_x')^2$ contribution to $\Delta N_\perp^2$ in (5), so that $\sigma \approx 4\sqrt{\varepsilon_0}\sigma_0(\tau, \eta - \eta')\delta(\Delta N_\parallel)$ where $d\tau(x) = dx/\sqrt{\varepsilon_0(x)}$, and

$$\sigma_0(\tau, \eta) = \frac{k_0^3 L_\perp^2}{4\sqrt{\varepsilon_0}} \Big\langle \frac{\delta n_e^2}{n_{e,c}^2} \Big\rangle e^{-\eta^2/(2\nu_\perp^2)}. \tag{7}$$

A straightforward calculations shows that equations (2) for a paraxial O-mode beam in slab geometry, with approximations (6) and (7), and for separable solutions, reduces to

$$\begin{cases} W = \dfrac{1}{2} f(\tau, y, \eta) g(\tau, z, \zeta) \delta\big(\xi + h(\eta)\big), \\ \partial_\tau f + \eta \partial_y f = S_0(f), \\ \partial_\tau g(\tau, z, \zeta) = 0, \end{cases} \tag{8}$$

with the convolution scattering operator

$$S_0(f) = \int_{-\infty}^{+\infty} \sigma_0(\tau, \eta - \eta')\big[f(\tau, y, \eta') - f(\tau, y, \eta)\big]d\eta'.$$

Equation (8) is the starting point for the derivation of our Eq. (12) below. From now on, no more approximations are introduced and the kinetic equation for f in (8) is dealt with rigorously. This model has been obtained as a special approximation of the radiative transfer model of the WKBeam code, in the case of paraxial beams propagating perpendicularly to the magnetic field in slab geometry and polarized in the O-mode. Alternatively, one could consider the paraxial approximation [48] of the Helmholtz equation for the electric field under the same conditions and derive the equation for the Wigner function. The two procedures are equivalent and give equation (8).

Since the scattering operator S_0 involve only a convolution, the kinetic equation for f can be solved via Fourier transform in both y and η. This leads to a linear advection-reaction equation which can be solved by the method of characteristics curves [49], with the solution

$$\hat{f}(\tau, p, q) = \exp\Big[\int_0^\tau \varphi_0\big(\tau', q+p(\tau-\tau')\big)d\tau'\Big]\hat{f}_0(p, q+p\tau).$$

In absence of density fluctuations, $\varphi_0 = 0$ and the Fourier transform can be inverted analytically; the result is the Wigner function for a Gaussian beam in slab geometry as it should be. In presence of density fluctuations, the analytical inversion of the Fourier transform is significantly more difficult, yet unnecessary, if one is only interested in computing the beam width.

In fact, we can compute "y-moments" of f, defined by

$$M_k(\tau) = \frac{\int y^k f(\tau, y, \eta)dyd\eta}{\int f(\tau, y, \eta)dyd\eta}, \tag{9}$$

directly form the Fourier transform $\hat{f}$. The beam width in particular is related to the second moment by

$$w^2(\tau) = 4M_2(\tau). \tag{10}$$

The proportionality factor follows from the fact that w is conventionally defined as the $1/e$ width of the electric field amplitude of the beam. On the other hand $\sqrt{2}M_2$ is the $1/e$ width of the energy density which is the square of the electric field.

Without density fluctuations ($\varphi_0 = 0$), (10) gives

$$\begin{aligned} w_{\rm GB}(\tau)^2 &= w_0^2\big[1 + \frac{2\tau}{R_0} + \frac{\tau^2}{L_R^2}\big] \\ &= w_*^2\big[1 + (\tau_*/\tau_R)^2\big], \end{aligned} \tag{11}$$

where $1/L_R^2 = 1/R_0^2 + 4/(k_0^2 w_0^4)$, $\tau = \tau_* - L_R^2/R_0$. The second expression in particular shows that $w_{\rm GB}$ is the standard width of a diffracting Gaussian beam in free space [50] with w_* being the beam width at the waist and with τ_R playing the role of the Rayleigh range. The effect of the plasma is entirely accounted for by the relation between the parameter τ and the physical position x along the slab. This relation between the solution in free space and in a plasma slab is known [46]. The fact that the radiative transfer model (2) captures a diffracting-beam solution can be interesting on itself as it clearly shows that the wave kinetic equation properly accounts for diffraction effects, even though the underlying Hamiltonian structure is the same as in geometric optics [51–53].

Using (9) and (10) one obtains, including the effect of density fluctuations,

$$w(\tau)^2 = w_{\rm GB}^2(\tau) + \int_0^\tau \frac{1}{L_\perp}\sqrt{\frac{2\pi}{\varepsilon_0}}\Big\langle\frac{\delta n_e^2}{n_{e,c}^2}\Big\rangle(\tau-\tau')^2 d\tau', \tag{12}$$

which is which is Eq. (1). The second term on the right-hand side describes the effect of scattering. It is always a broadening effect ($w^2 \geq w_{\rm GB}^2$), since the integral is positive. If we define the scattering contribution by $w_{\rm S} = \sqrt{w^2 - w_{\rm GB}^2}$, the total width is the length of the two-dimensional vector $\mathbf{w} = (w_{\rm GB}, w_{\rm S})$.

For the specific case of a uniform plasma equilibrium, all functions under the integral sign are constant and equation (12) reduces to

$$w(\tau)^2 = w_{\rm GB}^2(\tau) + \frac{1}{3L_\perp}\sqrt{\frac{2\pi}{\varepsilon_0}}\Big\langle\frac{\delta n_e^2}{n_{e,c}^2}\Big\rangle\tau^3.$$

One can see that the scattering term becomes dominant over diffraction for large τ. This result has been obtained by Sysoeva et at. [15] on the basis of the Helmholtz equation for a scalar wave field.

[1] E. Poli *et al.*, Nucl. Fusion **55**, 013023 (2015).
[2] C. M. Surko, R. E. Slusher, J. J. Schuss, R. R. Parker, I. H. Hutchinson, D. Overskei, and L. S. Scaturro, Phys. Rev. Lett. **43**, 1016 (1979).
[3] C. M. Surko and R. E. Slusher, Phys. Rev. Lett. **37**, 1747 (1976).
[4] S. Alberti, Nature Physics **3**, 376 (2007).
[5] M. Bornatici, R. Cano, O. De Barbieri, and F. Engelmann, Nucl. Fusion **23**, 1153 (1983).
[6] R. Prater, Phys. Plasmas **11**, 2349 (2004).
[7] G. Gantenbein, H. Zohm, G. Giruzzi, S. Günter, F. Leuterer, M. Maraschek, J. Meskat, Q. Yu, the ASDEX Upgrade Team, and the ECRH-Group AUG, Phys. Rev. Lett. **85**, 1242 (2000).
[8] I. G. J. Classen *et al.*, Phys. Rev. Lett. **98**, 035001 (2007).
[9] C. Lechte, G. D. Conway, T. Görler, and T. Happel, Plasma Science and Technology **22**, 064006 (2020).
[10] A. Snicker, E. Poli, O. Maj, L. Guidi, A. Koehn, H. Weber, G. D. Conway, M. A. Henderson, and G. Saibene, Nucl. Fusion **58**, 016002 (2018).

[11] C. Tsironis, A. G. Peeters, H. Isliker, D. Strintzi, I. Chatziantonaki, and L. Vlahos, Phys. Plasmas **16**, 112510 (2009).

[12] Y. Peysson, J. Decker, L. Morini, and S. Coda, Plasma Phys. Control. Fusion **53**, 124028 (2011).

[13] A. K. Ram, K. Hizanidis, and Y. Kominis, Phys. Plasmas **20**, 056110 (2013).

[14] A. K. Ram and K. Hizanidis, Phys. Plasmas **23**, 022504 (2016).

[15] E. V. Sysoeva, F. da Silva, E. Z. Gusakov, S. Heuraux, and A. Y. Popov, Nucl. Fusion **55**, 033016 (2015).

[16] S. Coda, J. Ahn, R. Albanese, S. Alberti, E. Alessi, S. Allan, H. Anand, G. Anastassiou, Y. Andrèbe, C. Angioni, *et al.*, Nucl. Fusion **57**, 102011 (2017).

[17] O. Chellaï, S. Alberti, M. Baquero-Ruiz, I. Furno, T. Goodman, B. Labit, O. Maj, P. Ricci, F. Riva, L. Guidi, *et al.*, Plasma Phys. Controll. Fusion **61**, 014001 (2018).

[18] O. Chellaï, S. Alberti, M. Baquero-Ruiz, I. Furno, T. Goodman, F. Manke, G. Plyushchev, L. Guidi, A. Koehn, O. Maj, *et al.*, Phys. Rev. Lett. **120**, 105001 (2018).

[19] F. Riva, C. Tsui, J. Boedo, P. Ricci, and T. Team, Physics of Plasmas **27**, 012301 (2020).

[20] F. Jenko, W. Dorland, M. Kotschenreuther, and B. Rogers, Physics of plasmas **7**, 1904 (2000).

[21] G. Merlo, S. Brunner, Z. Huang, S. Coda, T. Goerler, L. Villard, A. B. Navarro, J. Dominski, M. Fontana, F. Jenko, *et al.*, Plasma Physics and Controlled Fusion **60**, 034003 (2018).

[22] H. Weber, O. Maj, and E. Poli, EPJ Web of Conferences **87**, 01002 (2015).

[23] P. Blanchard, Y. Andrebe, H. Arnichand, R. Agnello, S. Antonioni, S. Couturier, J. Decker, T. D. K. DExaerde, B. Duval, I. Furno, *et al.*, Journal of Instrumentation **14**, C10038 (2019).

[24] A. Mosetto, F. D. Halpern, S. Jolliet, J. Loizu, and P. Ricci, Phys. Plasmas **20**, 092308 (2013).

[25] F. D. Halpern, S. Jolliet, J. Loizu, A. Mosetto, and P. Ricci, Phys. Plasmas **20**, 052306 (2013).

[26] H. M. Mott-Smith and I. Langmuir, Phys. Rev. **28**, 727 (1926).

[27] I. Hutchinson, *Principles of plasma diagnostics* (Cambridge University Press, 1987).

[28] O. Février, C. Theiler, H. De Oliveira, B. Labit, N. Fedorczak, and A. Baillod, Rev. Sci. Instrum. **89**, 053502 (2018).

[29] F. Nespoli, I. Furno, B. Labit, P. Ricci, F. Avino, F. Halpern, F. Musil, and F. Riva, Plasma Phys. Controll. Fusion **59**, 055009 (2017).

[30] The diagnostic was referred to as *X3TD* in previous publication. The name *O3TD* is more appropriate in this paper since the detection is now performed in ordinary mode.

[31] R. A. Fisher, Metron **1**, 3 (1921).

[32] O. Chellaï, *Millimeter-Wave Beam Scattering by Edge Turbulence in Magnetically-Confined Plasmas* (EPFL, Lausanne, 2019).

[33] C. Tsui, J. Boedo, J. Myra, B. Duval, B. Labit, C. Theiler, N. Vianello, W. Vijvers, H. Reimerdes, S. Coda, *et al.*, Phys. Plasmas **25**, 072506 (2018).

[34] I. Furno *et al.*, Phys. Plasmas **15**, 055903 (2008).

[35] G. Pereverzev, Physics of Plasmas **5**, 3529 (1998).

[36] Y. A. Kravtsov and Y. I. Orlov, goim (1990).

[37] *COMSOL RF Module User's Guide v5.2a*.

[38] T. Stix, The Theory of Plasma Waves, New York: McGraw-Hill (1962).

[39] A. Köhn, L. Guidi, E. Holzhauer, O. Maj, E. Poli, A. Snicker, and H. Weber, Plasma Phys. Controll. Fusion **60**, 075006 (2018).

[40] S. W. McDonald, Phys. Rev. A **43**, 4484 (1991).

[41] F. Riva, N. Vianello, M. Spolaore, P. Ricci, R. Cavazzana, L. Marrelli, and S. Spagnolo, Phys. of Plasmas **25**, 022305 (2018).

[42] T. Goerler, X. Lapillonne, S. Brunner, T. Dannert, F. Jenko, F. Merz, and D. Told, Journal of Computational Physics **230**, 7053 (2011).

[43] A. Medvedeva, C. Bottereau, F. Clairet, G. Conway, S. Heuraux, D. Molina, U. Stroth, A. U. Team, *et al.*, in *12th International Reflectometry Workshop (IRW 12)* (2015).

[44] A. Medvedeva, C. Bottereau, F. Clairet, P. Hennequin, U. Stroth, G. Birkenmeier, M. Cavedon, G. Conway, T. Happel, S. Heuraux, *et al.*, Plasma Phys. Controll. Fusion **59**, 125014 (2017).

[45] O. Maj *et al.*, Phys. Plasmas , to be submitted (2021).

[46] E. Poli, G. V. Pereverzev, and A. G. Peeters, Physics of Plasmas **6**, 5 (1999).

[47] S. W. McDonald, Physics Reports **158**, 337 (1988).

[48] G. V. Permitin and A. I. Smirnov, Zh. Eksp. Teor. Fiz. (JETP) **109**, 736 (1996).

[49] F. John, *Partial Differential Equations.* (Springer Berlin Heidelberg, 1980).

[50] H. Kogelnik and T. Li, Appl. Opt. **5**, 1550 (1966).

[51] L. A. Apresyan and Y. A. Kravtsov, *Radiation Transfer* (Taylor & Francis, 1996).

[52] G. R. Smith, D. R. Cook, A. N. Kaufman, A. H. Kritz, and S. W. McDonald, Physics of Fluids B: Plasma Physics **5**, 4299 (1993).

[53] O. Maj, Journal of Mathematical Physics **46**, 083510 (2005).